Nanoscale

PAPER

View Article Online
View Journal | View Issue

Cite this: *Nanoscale*, 2024, **16**, 11999

Spirobifluorene-BINOL-based microporous polymer nanoreactor for efficient 1*H*-tetrazole synthesis and iodine adsorption with facile charge transfer†

Flora Banerjee, Sudharanjan Bera, Tanushree Nath and Suman Kalyan Samanta *

Porous polymeric nanoreactors capable of multitasking are attractive and require a judicious design strategy. Herein, we describe an unusual approach for the synthesis of a porous polymer **SBF-BINOL-6** by *in situ* formation of the BINOL entity taking substituted naphthols and spirobifluorene as co-monomers with high yield (81%). The as-synthesized polymer exhibited nanotube and nanosphere-like morphology, thermal endurance up to 372 °C and a BET surface area as high as 590 $m^2\ g^{-1}$. The polymer endowed efficient loading of silver nanoparticles to generate **Ag@SBF6**, as confirmed from X-ray photoelectron spectroscopy and high-resolution transmission electron microscopy. **Ag@SBF6** was effectively used as a heterogeneous catalyst towards the [3 + 2] dipolar cycloaddition reaction for the synthesis of biologically important 5-substituted 1*H*-tetrazoles with yields in the range of 75–99% and recyclability for at least seven times without a significant decline in its catalytic efficiency. Additionally, a superior host–guest interaction by the polymer offered iodine adsorption in the vapour phase with a high uptake capacity of up to 4.0 g g^{-1}. Interestingly, the iodine-loaded polymer, **I_2@SBF6**, demonstrated iodine-promoted increased conductivity (1.3×10^{-3} S cm^{-1}) through facile charge transfer interactions.

Received 9th February 2024,
Accepted 9th May 2024

DOI: 10.1039/d4nr00599f

rsc.li/nanoscale

1. Introduction

To meet the global energy crisis, nuclear power generation has addressed a few major concerns with their zero-emission tendency and high-power generation rate, which may be estimated to further increase up to 715 GW(e) per annum within the next 25 years.[1,2] The classical uranium (^{238}U) fission process leads to the generation of several radioisotopes including ^{57}Se, ^{99}Tc, ^{129}I and ^{131}I.[3] Among them, radionuclide iodine (^{129}I) with an unusually long half-life (1.57×10^7 years) can pose challenges because it is a highly flowing gas and is soluble in water.[4,5] Meanwhile, the other radioisotope ^{131}I ($t_{1/2}$ = 8 days)[6] can cause carcinogenic effects and thyroid injury to the human body, and severe metabolic disorders to the entire aquatic biota through their biomagnification.[7,8] In the vapor phase, iodine mainly exists as I_2 in the molecular state,[9] although the existence of both iodide and triiodide has been reported.[7,8] Traces of both radioisotopes of iodine were detected to a significant extent when the unfortunate Chernobyl and Fukushima nuclear disasters took place. Hence, finding a suitable adsorbent for iodine vapor adsorption is of topical interest. Thus far, silver-containing zeolites, clay, and activated carbon along with metal–organic frameworks (MOFs) and porous organic frameworks (POFs) have been employed as potential materials for radioactive iodine capture.[10–16] Among these adsorbents, porous organic polymers (POPs) are a special class of polymer network type architecture, where the building units are covalently tethered with each other.[17–20] Such polymers with hierarchical porosity could overcome several shortcomings in iodine uptake, such as the selectivity, inadequate surface area, poor availability of binding sites and chemical stability, above all.[21,22] Geng *et al.* have illustrated the utility of biimidazole-based POPs with an exceptionally high iodine uptake capacity of up to 9.43 g g^{-1} in the vapor phase.[23] Wang *et al.* have reported the synthesis of a nitrogen and sulfur-rich POP with an iodine uptake of up to 2.86 g g^{-1} in the volatile state.[24] Recently, we have reported on amide-containing porous polymers exhibiting an iodine vapor uptake capacity of 3.53 g g^{-1}, which again emphasizes the crucial role played by the heteroatoms to trigger iodine adsorption.[25]

When considering the structural aspects of porous polymers, the spirobifluorene skeleton has certain unique features,

Department of Chemistry, Indian Institute of Technology Kharagpur, Kharagpur 721302, India. E-mail: sksamanta@chem.iitkgp.ac.in

†Electronic supplementary information (ESI) available: Detailed synthetic procedure along with characterisation details and experimental data. See DOI: https://doi.org/10.1039/d4nr00599f

such as its possession of a distinctive spiro-linkage connecting two orthogonal fluorene units. Commonly, spiro compounds often exhibit interesting steric and electronic properties due to the tetrahedral sp^3 carbon centre providing a non-coplanar arrangement of the connected rings.[26,27] Thus, a 90° knot can be incorporated into each repeating unit of the polymers made from such a precursor, preventing the packing of rigid polymer chains and generating a sizable, easily accessible free area. Often, POPs adorned with spirobifluorene units are more thermally robust than polymers with fluorene monomeric units.[19]

On the other hand, the inherent axial chirality in combination with anchoring –OH functionalities enable BINOL derivative-based insoluble microporous polymers to find wide applications in heterogeneous catalysis for various organic transformations. The Lin group illustrated the synthesis and employment of BINOL-based chiral crosslinked polymers loaded with a Ti active metal catalyst for Et_2Zn addition to substituted benzaldehydes.[28] In 2017, the Zhang group demonstrated the generation of self-supported BINOL-based porous carbazolic frameworks with improved catalytic activity exploring Ullmann C–N coupling chemistry, and applied the same approach in the asymmetric hydrogenation of 2-phenyl quinoline and 3-phenyl benzoxazine.[29]

In discussing the synthesis of multiple value-added N-heterocycles, it should be noted that tetrazoles belong to a class of popular intermediates prepared *via* [3 + 2] dipolar cycloaddition from benzonitrile.[30,31] They are common synthetic blocks for antifungal agents and other pharmaceuticals.[32] They have gained wide attention owing to their isosteric properties with carboxylic acids and their use in explosives, as well as various nitrogen-bearing aromatic heterocyclic compounds such as imidoylazides.[33] 5-Substituted 1*H*-tetrazoles have been previously prepared from isocyanides and hydrazoic acid, or cyclization between the ester of *ortho*-carboxylic acid and sodium azide, along with the salts of primary amines.[34–36] Various other methods involving Lewis acid catalysts, *e.g.*, In $(OTf)_3$, $AgNO_3$, $Fe(OAc)_2$ and natrolite zeolite, were reported in the literature.[37–40] However, most of these processes lack long-term stability and recoverability of the catalyst, while compromising the catalytic efficiency in some cases as well.

Metallic nanoparticles are often endowed with potential applications owing to their exalted surface/volume ratio, which may result in higher accessibility of active sites.[41] Unfortunately, there are drawbacks associated with their use, which may occur owing to their poor thermodynamic stability, *i.e.*, high surface energy.[41] For this purpose, the choice of a potential capping ligand is supposed to play a pivotal role in imparting stability to the entire system *via* electron-donating immobilization.[42] However, the lack of a proper support may have consequences of metal nanoparticle aggregation and the formation of a bulk mass with dropped recyclability and catalytic activity. In order to alleviate such possibilities, heterogeneous catalysis within nanoreactors could find efficacious support to simultaneously achieve persistent activity and improved reusability.[43]

Silver nanoparticles (AgNPs) have attracted great interest owing to their improved physicochemical and biological properties, as compared to their macroscale counterparts.[44] Their tendency towards oxidation is less as compared to the main group transition elements. Thus, the stability is much more pronounced, displaying higher surface reactivity in the long-run. AgNPs can be generated biologically, physically or by chemical methods.[45,46] Among them, the nanoparticle immobilization within the solid support turns out to be potentially useful to inhibit their tendency towards agglomeration. Hence, extensive efforts were made towards stabilizing AgNPs for various reactions, such as the reduction of nitrophenols or catalytic fixation of CO_2 with propargyl alcohols.[47] However, the synthesis of 1*H*-tetrazoles has been scarcely reported with AgNPs supported in the organic host.

Herein, a synthetic strategy was delineated involving the generation of a BINOL-based porous polymer with a spirobifluorene core, where the BINOL formation was achieved *in situ* during the final polymerization step. Interestingly, this polymer acted as an excellent host in nanoscale towards the loading of AgNPs *via* the reduction of silver nitrate. The as-synthesized **Ag@SBF6** could act as a nanocatalyst towards the synthesis of value-added N-heterocycles, *i.e.*, 5-substituted-1*H*-tetrazoles with good to excellent yields. Additionally, a superior host–guest interaction offered by the polymer led to the high uptake of iodine from the vapor phase. Thereafter, the iodine-loaded POP was demonstrated to have increased conductivity upto 1.3×10^{-3} S cm^{-1} *via* facile charge transfer.

2. Results and discussion

The spirobifluorene-based porous polymer **SBF-BINOL-6** was synthesized *via* $FeCl_3$-mediated oxidative coupling polymerization from a naphthol-containing monomer. For this purpose, borylation of the commercially available 6-bromo-2-naphthol was achieved first with 96% yield following our previous report,[48] and then Suzuki–Miyaura cross-coupling with 2,2′,7,7′-tetrabromospirobifluorene produced the monomer **1** (68% yield) (Scheme 1 and Scheme S1, ESI†). The chemical

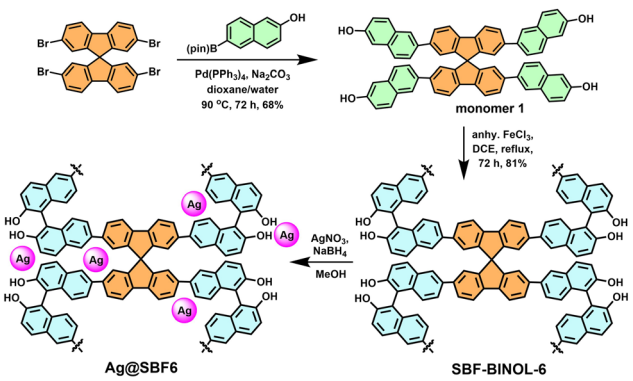

Scheme 1 Synthesis route to spirobifluorene and BINOL-containing polymer **SBF-BINOL-6** and the AgNPs-loaded polymer **Ag@SBF6**.

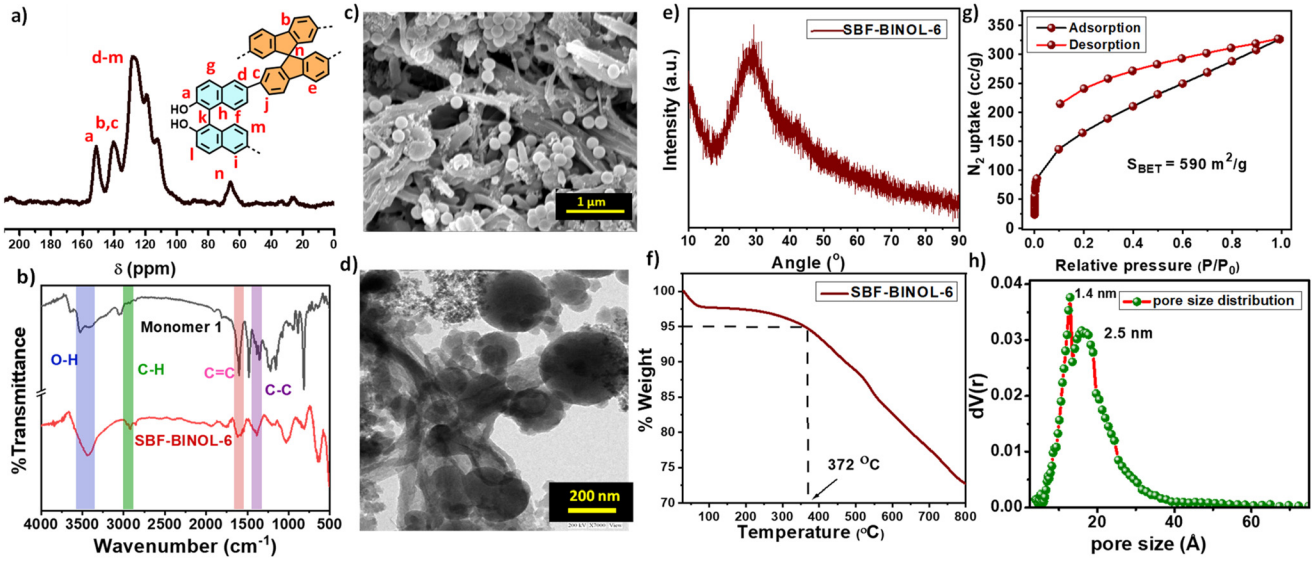

Fig. 1 (a) ^{13}C CP/MAS NMR spectrum, (b) FT-IR spectra along with monomer **1**, (c) SEM image, (d) TEM image, (e) PXRD pattern, (f) TGA profile, (g) N_2 adsorption isotherm at 77 K, and (h) pore size distribution of **SBF-BINOL-6**.

structure of monomer **1** was confirmed with ^{1}H, ^{13}C NMR, FT-IR and mass spectra (Fig. 1b and Fig. S1, S2, ESI†). The $FeCl_3$-mediated oxidative coupling polymerization afforded **SBF-BINOL-6** with 81% yield (Scheme S2, ESI†).

Key structural features were obtained for **SBF-BINOL-6** using solid state ^{13}C CP/MAS NMR and FT-IR spectroscopy. Solid-state NMR showed the peaks at 113–116 ppm, 123–129 ppm and 152 ppm, corresponding to aryl carbons rising from the BINOL skeleton within the network, while the spirobifluorene carbons were located at 141, 123–129 and 67 ppm (Fig. 1a).[19,48] FT-IR spectra of the polymer highlighted the O–H stretching peak at 3425 cm^{-1}, 1559 cm^{-1} for –C=C and 1284 cm^{-1} for –C–C stretching, which matches well with that of monomer **1**, ascertaining the presence of the monomer within the polymer skeleton, *i.e.*, effective polymerization *via* $FeCl_3$-mediated oxidative coupling (Fig. 1b).

Scanning electron microscope (SEM) images of **SBF-BINOL-6** highlighted the presence of aggregated particles, along with hollow rod and solid sphere-like morphological traits (Fig. 1c). Meanwhile, the transmission electron micrograph (TEM) study showed an aggregate of arranged particles having a spherical shape (Fig. 1d). Energy-dispersive X-ray (EDAX) absorption patterns disclosed the absence of Fe in these polymers, indicating that the $FeCl_3$ catalyst residues were completely eliminated after rigorous stirring with HCl (Fig. S3, ESI†). Powder X-ray diffraction (PXRD) patterns of POP revealed the amorphous nature originating from random polymerisation, *i.e.*, rapid cross-linking (Fig. 1e). The existence of a broad hump near 25° may be attributed to π–π stacking between the aromatic linkers.[49] Thermogravimetric analysis (TGA) indicated the thermal stability of **SBF-BINOL-6** up to 372 °C with a weight loss of 5%, *i.e.*, ability to work under harsh environments (Fig. 1f).

The porosity of the as-synthesized polymer was inspected with the N_2 adsorption–desorption isotherm at 77 K. **SBF-BINOL-6** exhibited a sharp increase in N_2 uptake at the low pressure region ($P/P_0 \sim 0.1$), which is attributed to a large excess of micropores present having an ink-bottle like topology (Fig. 1g). A large hysteresis loop with H2-type pattern from $P/P_0 \sim 0.5$–0.8 could result from the rigidity imparted by spirobifluorene, as well as the binaphthalene backbone of the network, affecting the reversibility of the physisorption process. The non-localised density functional theory (NLDFT) method-assisted pore size distribution showed the maxima located at 1.4 nm and 2.5 nm, depicting the presence of both micro- and mesopores within the network, confirming the hierarchical porosity of this POP (Fig. 1h). **SBF-BINOL-6** offered a moderately high BET surface area of 590 $m^2\ g^{-1}$. Interestingly, the micropore surface area was found to be 265 $m^2\ g^{-1}$, which confirmed that nearly 50% of the total pores were covered by micropores. The total pore volume was ~0.34 $cm^3\ g^{-1}$.

BINOL-based porous polymers are well-documented for their chelating property towards different metal ions, and thus provide stability to them for effective utilisation in a heterogeneous catalyst. In our case, the *in situ* generation of AgNPs was performed by the $NaBH_4$-mediated reduction of $AgNO_3$, keeping **SBF-BINOL-6** as the host (*cf.* Experimental section, ESI†). For AgNPs loading, 10 mg of **SBF-BINOL-6** was dispersed in 10 mL of a water : methanol mixture (1 : 1), followed by adding 3 mL of 10 mM aqueous solution of $AgNO_3$, along with 5 mL of 10 mM methanolic solution of $NaBH_4$ to perform the reduction.[50] The resulting polymer was characterised by FT-IR spectroscopy to check the structural integrity of the polymer. A small blue shift of 15–20 cm^{-1} in the O–H stretching and C=C stretching frequencies were observed, indicating the participation of these units in AgNPs stabilisation (Fig. S4, ESI†).[47]

The thermal analysis indicated thermal stability up to 272 °C for the AgNPs-incorporated polymer, which could be beneficial for its operation under high-temperature reaction conditions (Fig. S5, ESI†). The AgNP-loaded polymer, namely **Ag@SBF6**, was characterized with SEM, showing an aggregate of small particles over the surface of the POP (Fig. 2a). The EDAX pattern highlighted the presence of Ag with uniform distribution over the POP matrix (Fig. 2b–d). Further insight into the nanoparticle distribution over the polymer host was unveiled with TEM, highlighting the uniform presence of the nanoparticles without any agglomeration over the polymer (Fig. 2e). To our delight, the crystalline fringes were also spotted on the micrograph with a crystallite size of 0.98 nm (Fig. 2f). Furthermore, the silver atomic interlayers were identified using the selected area electron diffraction (SAED) pattern with a spacing of 8.76 nm (Fig. 2g). The particle size distribution histogram exhibited a narrow distribution for the average particle size of 23 nm (Fig. 2h). The BET surface area was drastically reduced upon successful incorporation of AgNPs, which is in accordance with that of previous reports.[41] The BET surface area was 262 m^2 g^{-1} (Fig. 3a), along with a pore size distribution mainly concentrated at the microporous region (1.1–1.4 nm) (Fig. 3b). This fact, in other words, confirmed that the AgNPs occupied the mesoporous channels to facilitate catalytic mass transfer.

The oxidation state of Ag in the as-prepared **Ag@SBF6** was deduced using X-ray photoelectron spectroscopy (XPS) studies, which showed peaks at 368.4 eV ($3d_{5/2}$) and 374.4 eV ($3d_{3/2}$) corresponding to Ag(0), thus confirming the complete conversion of Ag(I) to Ag(0) during the $NaBH_4$-mediated reduction (Fig. 3c).[51,52] The C 1s deconvoluted spectrum showed both binding energies corresponding to C=C at 282.9 eV and C–C at 284.1 eV, and for O 1s at 531.9 eV standing for the spirobifluorene moiety and the BINOL –OH moiety, respectively

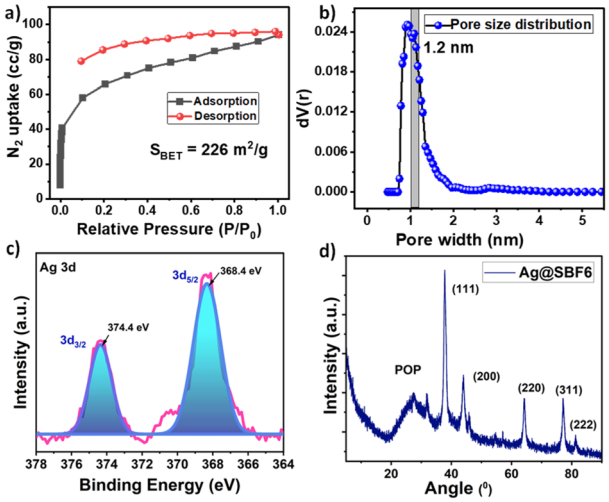

Fig. 3 (a) BET adsorption isotherm, (b) NLDFT-based pore size distribution curve, (c) Ag deconvoluted XPS and (d) PXRD pattern for **Ag@SBF6**.

(Fig. S6, ESI†). The PXRD profile evidenced the retention of the hump-like peak near 25° and the rise of sharp peaks at 38°, 45°, 64°, 78°, and 81°. This broad hump at 25° may have stemmed from the amorphous nature of **SBF-BINOL-6**, as observed in the native polymer, and the sharp peaks appeared owing to the presence of (111), (200), (220), (311) and (222) crystal planes of AgNPs, indicating that the fcc array of silver was unaltered within the nanocatalyst (Fig. 3d).[53,54] The presence of Ag nanoparticles was further validated with the UV-vis diffused reflectance spectrum (DRS) of **Ag@SBF6**, unraveling a small shoulder peak at 450 nm corresponding to the surface plasmon resonance signal of Ag(0) (Fig. S7, ESI†). The

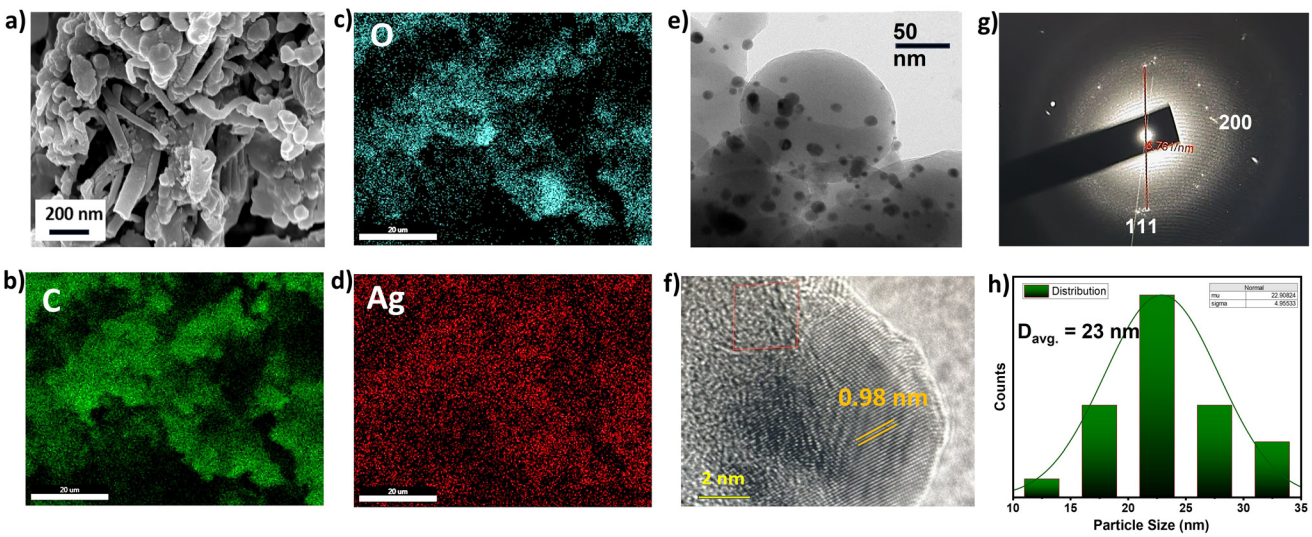

Fig. 2 (a) SEM image of **Ag@SBF6**. Elemental mapping images of **Ag@SBF6** showing (b) carbon; (c) oxygen; and (d) silver. (e) TEM micrograph, (f) crystalline fringes, and (g) SAED pattern of **Ag@SBF6** from HRTEM. (h) Particle size distribution profile of **Ag@SBF6** obtained from TEM.

weight% of silver loading within the polymer was analyzed with the help of TGA under air. The data revealed 18.12% silver loading within the porous polymer after nanoparticle loading (Fig. S8, ESI†).[43]

The AgNPs-loaded catalyst was tested for synthesizing tetrazoles *via* click reaction (*cf.* Experimental section, ESI†). The catalytic properties of the as-synthesized **Ag@SBF6** were first tested for the synthesis of 1*H*-tetrazole utilizing the principle of [3 + 2] dipolar cycloaddition chemistry. Benzonitrile and sodium azide were taken as the model substrate for performing the reaction (Table 1). Several solvents were screened to maximise the yield of the product (Table S1, ESI†). Thereafter, the nonpolar solvents were eliminated due to much less conversion to the products (10–25%). Unfortunately, the product formation was also much less when water was tested as a green solvent. In contrast, the polar protic solvents showed much better yield, where dimethyl sulfoxide (DMSO) and dimethylformamide (DMF) furnished the tetrazole with 60% and nearly quantitative yield, respectively. Therefore, DMF was chosen for further catalysis reactions. The scope of the catalyst in the click reaction was expanded with various substrates and optimized reaction conditions.

Optimization of the substrate scope revealed that upon increasing the nature of the electron-withdrawing group in the *para* position of the substrate, the % yield of the product increased. For *p*-methoxy benzonitrile, 78% yield was obtained. Meanwhile, for *p*-hydroxy benzonitrile, 92% yield was achieved (Table 1). To evaluate the mechanistic path, control studies were performed with the host polymer **SBF-BINOL-6** as the catalyst, yielding only a trace amount of tetrazole, which further indicated the crucial role of AgNPs loaded on the polymer matrix as the active heterogeneous catalyst. This trend is consistent with the mechanism of the [3 + 2] dipolar cycloaddition reaction, which is initiated with the activation of –CN from benzonitrile with the Ag(0) species immobilized on **SBF-BINOL-6** *via* coordinate bond formation with the –CN nitrogen atom from the benzonitrile moiety, followed by nucleophilic attack by the azide, and lastly annulation furnishing 1*H*-tetrazoles (Scheme 2). It can be considered

Table 1 Substrate scope for the synthesis of 1*H*-tetrazoles with the **Ag@SBF6** catalyst

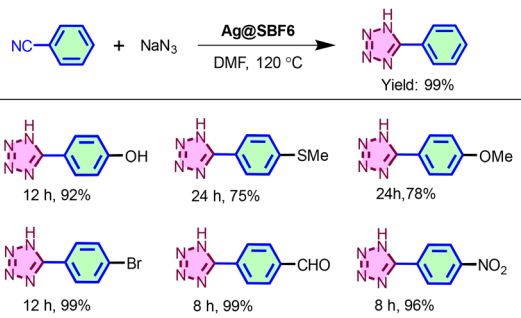

Reaction conditions: benzonitrile (1 mmol), NaN_3 (1.5 mmol), DMF (3 mL) and catalyst, **Ag@SBF6** (5 mg). Yields are reported for isolated products.

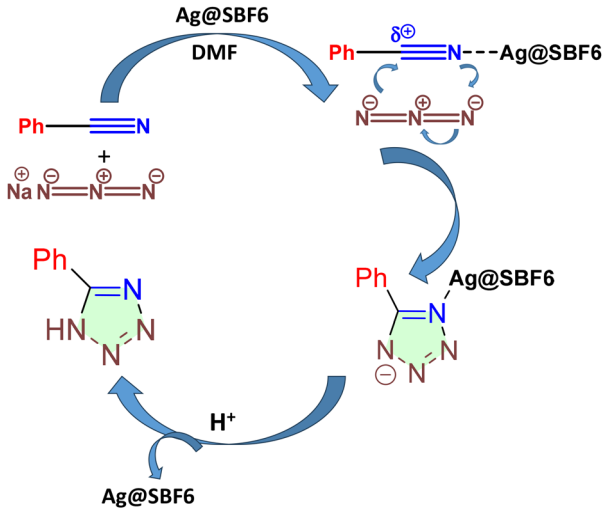

Scheme 2 Plausible mechanism for the synthesis of 1*H*-tetrazole.

that the presence of the electron-donating group at the *p*-position of the aromatic ring resulted in a significant drop in the electron affinity of the nitrile carbon, which further inhibited the nucleophilic attack of azide, and thus affected the product yield. The activation of –CN was further testified with DFT-based calculations of natural bond orbital (NBO) charges for each atom. The results indicated an increase in the partially positive charge (δ^+) over the –CN carbon atom when the terminal N atom is bonded with the Ag(0) species (Fig. S9, ESI†). This observation supported the lower reaction time observed for the benzonitriles with the electron-withdrawing substituent compared to that of the electron-donating ones.

The hot filtration test was performed to test the metal nanoparticle leaching within the solution during the catalytic cycle. The heterogeneous catalyst was filtered using a pre-heated Celite pad after 2 h from starting the reaction, and then the filtrate was allowed to react further. After the stipulated time, no further conversion took place and only 29% product was formed. This observation eliminated the possibility of metal nanoparticles leaching within the reaction media. These results were aligned with the durability of our as-developed nanoreactor, where the strong host–guest interaction facilitated the superior catalytic activity.

For practical catalytic applications, the regeneration and reuse of a heterogeneous catalyst is of paramount importance. Once the reaction was over, the catalyst was separated *via* simple gravity filtration method. After washing several times with methanol and acetone, it was put through the next cycle. Strikingly, it could offer a recyclability of up to seven runs without considerably losing its catalytic efficiency (Fig. S10, ESI†). The catalyst was checked with FESEM and EDAX, which confirmed the morphological integrity after recycling (Fig. S11, ESI†). To our delight, our as-synthesized **Ag@SBF6** showed improved recyclability with comparable catalytic efficiency with low catalyst loading to that of the previous reports with bare AgNPs as the catalyst for similar reactions.[38] This could presumably result either from the agglomeration in the case of

AgNPs in the absence of any solid support, or the tendency of metal leaching within the reaction mixture in the absence of any capping ligand or stabilizing system.

Inspired by the fact that, silver-loaded species often exhibit high binding affinity towards iodine, **Ag@SBF6** was utilised as an adsorbent for iodine in the vapor phase. For iodine uptake, a pre-weighed polymer adsorbent was kept at 75 °C in the presence of iodine vapor under ambient pressure (*cf.* Experimental section, ESI†).[24,55] The iodine uptake in the vapor phase was monitored through gravimetric analysis by measuring the weight of the polymer after different time intervals with the change in the appearance of the polymer from a yellowish to brown-black color. The uptake capacity was calculated with the following formula:

$$Q = [(m_2 - m_1)/m_1] \times 100 \text{ wt\%}$$

where Q is the iodine uptake capacity, and m_1 and m_2 are the mass of the POP samples before and after iodine capture, respectively. Interestingly, the AgNPs-loaded POP showed an adsorption capacity of 2.13 g g^{-1} (Fig. 4). For a comparison, under similar conditions, when **SBF-BINOL-6** was utilised as an adsorbent for iodine in the vapor phase, the uptake capacity surprisingly reached its maxima at 4.0 g g^{-1} within 10 hours. This indicated a poor availability of binding sites towards iodine after AgNPs loading. Moreover, the heteroatom-rich pores, *i.e.*, the adsorbents containing –OH rich functional groups and aromatic backbone, were demonstrated to be a potential adsorbent towards iodine uptake for the Lewis acidic nature of iodine. This cites the first example of a BINOL-based POP as an efficacious platform for iodine uptake from the vapor phase. The amount of iodine loaded within the native polymer **SBF-BINOL-6** was further investigated with TGA under an argon atmosphere, which clearly displayed 39 wt% additional loss in the presence of sorbed iodine for 9.012 mg of polymer. Thus, the total iodine loaded within the iodine loaded polymer (**I_2@SBF6**) was found to be 351 wt%, as obtained from the thermal analysis (Fig. S12, ESI†).

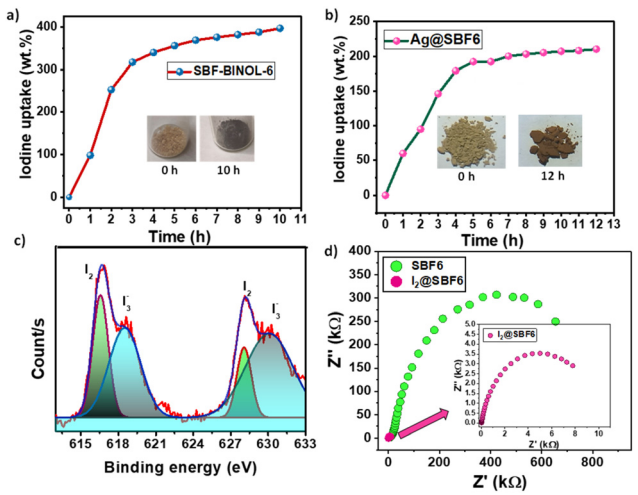

Fig. 4 Iodine vapor uptake with time for (a) **SBF-BINOL-6**; (b) **Ag@SBF6**. (c) Deconvoluted XPS spectra for iodine in **I_2@SBF6**. (d) The Nyquist plot for **SBF-BINOL-6** and **I_2@SBF6** (inset).

The iodine-loaded POP, **I_2@SBF6**, was characterised with UV-vis-NIR diffused reflectance spectra (DRS), XPS, EDX, PXRD, EPR and Raman spectroscopy. The presence of iodine was confirmed from the elemental mapping highlighting the uniform distribution of iodine over the POP (Fig. S13, ESI†). The solid-state diffused reflectance spectra of the bare polymer along with **I_2@SBF6** were monitored to see the change in the absorption properties. The absorption was significantly red-shifted, confirming the successful iodine loading within the polymer (Fig. S14, ESI†). On the other hand, the PXRD profile did not indicate any distinct change even after iodine incorporation, which indicated no such alteration in structure of the parent POP (Fig. S15, ESI†). The XPS profile guided us to confirm the oxidation state of the iodine bound to the polymer matrix. The peaks at 615.9 and 629.1 eV correspond to molecular I_2, and the peaks at 619.1 and 630.5 eV correspond to I_3^- and polyiodide ions (Fig. 4c). The Raman spectra of **I_2@SBF6** featured clear peaks at 109 and 168 cm^{-1}, indicating the distinct charge transfer that resulted in the formation of I_3^- and polyiodide ions along with I_2, which was not evident in the host polymer **SBF-BINOL-6** (Fig. S16, ESI†).[56] The Raman spectra also closely resembled the Raman band of I_2 in the solid/gas state, which is located near 180 cm^{-1} and possesses A_g/A_{1g} symmetry, indicating the presence of I_2 in the molecular state as well.[57] A strong red shift of 18 cm^{-1} was observed compared to the conventional I_3^- band (150 cm^{-1}). This was presumably due to the strong interaction with the polymer host.[58] Similarly, the EPR pattern confirmed the existence of host–guest charge transfer from the polymer to iodine upon exposure to iodine vapor, displaying a single Lorentzian line for **I_2@SBF6**, while solid iodine was found to be EPR-silent (Fig. S17, ESI†).[59] The charge transfer phenomena corroborated well with the theoretical calculations. The electrostatic potential surface mapping between our BINOL model unit and molecular iodine clarified that the electrostatic attractive force could be a guiding factor towards imparting a stabilization energy of 34.5 kcal mol^{-1} (Fig. S18, ESI†). The binding energy data helped us pave the path towards a plausible interaction site for iodine, which was BINOL in our case. The electronic distribution for HOMO, LUMO, LUMO+1 and LUMO+2 was modelled with the help of density functional theory-based study. The electron density at different energy levels indicated the propensity of charge transfer complex formation between iodine and BINOL model unit (Fig. S19, ESI†). Instead of iodine, when triiodide was taken as the model guest molecule, the charge separation was more prominent in the host–guest inclusion complex (Fig. S20, ESI†).

Results obtained from the EPR and XPS profile, along with theoretical calculations, suggested the possibility of a charge transfer complex formation between our polymer host and iodine. To gain deeper insight, the iodine-loaded POP was put through the electrochemical tests to inspect the effect of iodine or triiodide binding on the host network. In this regard, the electrochemical impedance spectra (EIS) of the polymer **SBF-BINOL-6** denoted a significant drop in charge-

transfer resistance after the loading of iodine vapor within the polymer. Interestingly, the charge transfer resistance value was similar under both illuminated and dark condition, which attested that the chances of photogenerated conductivity, *i.e.*, charge carrier migration could have minimal contribution towards the overall EIS response (Fig. S21, ESI†). These experimental facts suggest an efficient host–guest charge transfer upon the loading of iodine within the spirobifluorene-based porous polymer, which further elevated their conductivity through dropping the R_{ct} by 100-fold (Fig. 4d).[58] The profound reason could be the presence of triiodide or polyiodide ions adhered to the surface, leading to the remarkably increased charge transfer-mediated conductivity (1.3×10^{-3} S cm^{-1}) of the polymer (*cf.* Experimental section, ESI†).

The iodine-loaded polymer was washed with ethanol and filtered for regeneration of the adsorbent. The recovered polymer was successfully reused up to four successive runs without significantly affecting their maximum uptake capacity (Fig. S22, ESI†). Their morphological and structural features were tested with FESEM and PXRD, which matched well with that of the fresh polymer **SBF-BINOL-6** (Fig. S23, ESI†).

3. Conclusions

For the first time, we have furnished the hypercrosslinked polymer bearing spirobifluorene as well as BINOL *via in situ* formation of the BINOL entity. The polymer exhibited hierarchically porous channels stemming from spirobifluorene along with naphthoic-OH rich pores, which may endow superior stability for the Ag nanoparticles. Thus, AgNPs-loaded **SBF-BINOL-6** was employed towards the production of 5-substituted-1*H*-tetrazoles by [3 + 2] dipolar cycloaddition reaction with a yield up to 99% over a broad range of substrates. The catalyst could be recycled at least seven runs without considerably losing the catalytic performance. The polymer was further applied towards iodine capture from the vapor state (4.0 g g^{-1}). Although, the AgNPs-loaded polymer could not facilitate higher iodine uptake (2.1 g g^{-1}), presumably stemming from the pore blocking effect of AgNPs. Our theoretical study brought insight into the plausible charge transfer, which was supported by Raman, EPR and XPS spectral data. The iodine-loaded polymer exhibited remarkably increased conductivity (1.3×10^{-3} S cm^{-1}) as compared to the parent POP, **SBF-BINOL-6**. The conductivity experiments with EIS pattern depicted facile charge transfer with 100-fold drop in the R_{ct} value. Therefore, these studies demonstrate that the BINOL-based POP containing a superior spirobifluorene moiety holds tremendous potential towards their multifaceted applications in heterogeneous catalysis and environmental remediation.

Author contributions

F. B. performed the synthesis and characterization of the polymer, iodine uptake studies and writing the manuscript. S. B. and T. N. performed the catalytic studies. S. K. S. designed the project and supervised all the experiments. The manuscript was written with permission from all the authors.

Conflicts of interest

There are no conflicts to declare.

Acknowledgements

F. B. acknowledges MoE, Govt. of India for the PMRF fellowship. S. B. is thankful to IIT Kharagpur for fellowship. We are thankful to Paramshakti supercomputing facility, IIT Kharagpur for computational studies and Central Research Facility (CRF), IIT Kharagpur for the instrumental facilities. S. K. S. acknowledges SERB, DST (SRG/2019/000922) for funding this research works. This article is dedicated to the 65th birthday of Professor Santanu Bhattacharya.

References

1 L. Zhan, Y. Bo, T. Lin and Z. Fan, *Energy Strategy Rev.*, 2021, **34**, 100630.
2 *Energy, Electricity and Nuclear Power Estimates for the Period up to 2050*, INTERNATIONAL ATOMIC ENERGY AGENCY, Vienna, 2020.
3 D. F. Sava, M. A. Rodriguez, K. W. Chapman, P. J. Chupas, J. A. Greathouse, P. S. Crozier and T. M. Nenoff, *J. Am. Chem. Soc.*, 2011, **133**, 12398–12401.
4 W. Xie, D. Cui, S.-R. Zhang, Y.-H. Xu and D.-L. Jiang, *Mater. Horiz.*, 2019, **6**, 1571–1595.
5 K. S. Subrahmanyam, D. Sarma, C. D. Malliakas, K. Polychronopoulou, B. J. Riley, D. A. Pierce, J. Chun and M. G. Kanatzidis, *Chem. Mater.*, 2015, **27**, 2619–2626.
6 Y. S. Shimamoto, Y. Takahashi and Y. Terada, *Environ. Sci. Technol.*, 2011, **45**, 2086–2092.
7 F. C. Küpper, M. C. Feiters, B. Olofsson, T. Kaiho, S. Yanagida, M. B. Zimmermann, L. J. Carpenter, G. W. Luther III, Z. Lu, M. Jonsson and L. Kloo, *Angew. Chem., Int. Ed.*, 2011, **50**, 11598–11620.
8 A. Saiz-Lopez, J. M. C. Plane, A. R. Baker, L. J. Carpenter, R. von Glasow, J. C. Gómez Martín, G. McFiggans and R. W. Saunders, *Chem. Rev.*, 2012, **112**, 1773–1804.
9 P. Wang, Q. Xu, Z. Li, W. Jiang, Q. Jiang and D. Jiang, *Adv. Mater.*, 2018, **30**, 1801991.
10 K. W. Chapman, P. J. Chupas and T. M. Nenoff, *J. Am. Chem. Soc.*, 2010, **132**, 8897–8899.
11 B. Riebe, S. Dultz and C. Bunnenberg, *Appl. Clay Sci.*, 2005, **28**, 9–16.
12 J. Huve, A. Ryzhikov, H. Nouali, V. Lalia, G. Augé and T. J. Daou, *RSC Adv.*, 2018, **8**, 29248–29273.
13 A. Hassan and N. Das, *ACS Appl. Polym. Mater.*, 2023, **5**, 5349–5359.

14 P. Chen, X. He, M. Pang, X. Dong, S. Zhao and W. Zhang, *ACS Appl. Mater. Interfaces*, 2020, **12**, 20429–20439.
15 X. Li, Y. Peng and Q. Jia, *Sep. Purif. Technol.*, 2020, **236**, 116260.
16 X. Li, H. Xiong and Q. Jia, *ACS Appl. Mater. Interfaces*, 2019, **11**, 46205–46211.
17 S. Bera, S. Sau, N. Kumar and S. K. Samanta, *ACS Appl. Nano Mater.*, 2024, **7**, 529–538.
18 S. Sau, F. Banerjee and S. K. Samanta, *ACS Appl. Nano Mater.*, 2023, **6**, 11679–11688.
19 A. Modak, Y. Maegawa, Y. Goto and S. Inagaki, *Polym. Chem.*, 2016, **7**, 1290–1296.
20 S. Sau and S. K. Samanta, *Chem. Commun.*, 2023, **59**, 635–638.
21 C. Pei, T. Ben, S. Xu and S. Qiu, *J. Mater. Chem. A*, 2014, **2**, 7179–7187.
22 X. Qian, B. Wang, Z.-Q. Zhu, H.-X. Sun, F. Ren, P. Mu, C. Ma, W.-D. Liang and A. Li, *J. Hazard. Mater.*, 2017, **338**, 224–232.
23 T. Geng, C. Zhang, M. Liu, C. Hu and G. Chen, *J. Mater. Chem. A*, 2020, **8**, 2820–2826.
24 H. Wang, N. Qiu, X. Kong, Z. Hu, F. Zhong, Y. Li and H. Tan, *ACS Appl. Mater. Interfaces*, 2023, **15**, 14846–14853.
25 S. Bera, K. Garg and S. K. Samanta, *ACS Appl. Nano Mater.*, 2024, **7**, 1797–1803.
26 Y. Liu, C. Wu, Q. Sun, F. Hu, Q. Pan, J. Sun, Y. Jin, Z. Li, W. Zhang and Y. Zhao, *CCS Chem.*, 2020, **3**, 2418–2427.
27 Y. Wang, Y. Liu, H. Li, X. Guan, M. Xue, Y. Yan, V. Valtchev, S. Qiu and Q. Fang, *J. Am. Chem. Soc.*, 2020, **142**, 3736–3741.
28 L. Ma, M. M. Wanderley and W. Lin, Highly Porous Cross-Linked Polymers for Catalytic Asymmetric Diethylzinc Addition to Aldehydes, *ACS Catal.*, 2011, **1**, 691–697.
29 X. Zhang, A. Kormos and J. Zhang, *Org. Lett.*, 2017, **19**, 6072–6075.
30 R. N. Butler, in *Comprehensive Heterocyclic Chemistry*, ed. A. R. Katritzky and C. W. Rees, Pergamon, Oxford, 1984, pp. 791–838.
31 Z. P. Demko and K. B. Sharpless, *J. Org. Chem.*, 2001, **66**, 7945–7950.
32 S.-Q. Wang, Y.-F. Wang and Z. Xu, *Eur. J. Med. Chem.*, 2019, **170**, 225–234.
33 R. J. Herr, *Bioorg. Med. Chem.*, 2002, **10**, 3379–3393.
34 T. Jin, S. Kamijo and Y. Yamamoto, *Tetrahedron Lett.*, 2004, **45**, 9435–9437.
35 A. K. Gupta, C. H. Song and C. H. Oh, *Tetrahedron Lett.*, 2004, **45**, 4113–4116.
36 F. G. Fallon and R. M. Herbst, *J. Org. Chem.*, 1957, **22**, 933–936.
37 D. Kundu, A. Majee and A. Hajra, *Tetrahedron Lett.*, 2009, **50**, 2668–2670.
38 P. Mani, C. Sharma, S. Kumar and S. K. Awasthi, *J. Mol. Catal. A: Chem.*, 2014, **392**, 150–156.
39 J. Bonnamour and C. Bolm, *Chem. – Eur. J.*, 2009, **15**, 4543–4545.
40 D. Habibi, M. Nasrollahzadeh and T. A. Kamali, *Green Chem.*, 2011, **13**, 3499–3504.
41 B. K. Chandra, S. Pal, A. Majee and A. Bhaumik, *Mol. Catal.*, 2022, **531**, 112686.
42 M. J. MacLeod and J. A. Johnson, *J. Am. Chem. Soc.*, 2015, **137**, 7974–7977.
43 S. Bera, F. Banerjee and S. K. Samanta, *ACS Appl. Nano Mater.*, 2023, **6**, 15002–15011.
44 L.-s. Li, J. Hu, W. Yang and A. P. Alivisatos, *Nano Lett.*, 2001, **1**, 349–351.
45 L. Nair and C. Laurencin, *J. Biomed. Nanotechnol.*, 2007, **3**, 301–316.
46 Y. Zhang, H. Peng, W. Huang, Y. Zhou and D. Yan, *J. Colloid Interface Sci.*, 2008, **325**, 371–376.
47 A. Roy, N. Haque, R. Chatterjee, S. Biswas, A. Bhaumik, M. Sarkar and S. M. Islam, *New J. Chem.*, 2023, **47**, 6673–6684.
48 F. Banerjee and S. K. Samanta, *Mater. Chem. Front.*, 2023, **7**, 689–697.
49 D. Shetty, S. Boutros, T. Skorjanc, B. Garai, Z. Asfari, J. Raya and A. Trabolsi, *J. Mater. Chem. A*, 2020, **8**, 13942–13945.
50 S. Bera, F. Banerjee and S. K. Samanta, *ChemNanoMat*, 2023, **9**, e202300088.
51 N. Perkas, M. Shuster, G. Amirian, Y. Koltypin and A. Gedanken, *J. Polym. Sci., Part A: Polym. Chem.*, 2008, **46**, 1719–1729.
52 Z. Huang, H. Jiang, P. Liu, J. Sun, D. Guo, J. Shan and N. Gu, *J. Mater. Chem. A*, 2015, **3**, 1925–1929.
53 J. Liu, J. Cui, F. Vilela, J. He, M. Zeller, A. D. Hunter and Z. Xu, *Chem. Commun.*, 2015, **51**, 12197–12200.
54 H. B. Erdem and S. Çetinkaya, *Heliyon*, 2022, **8**, e10659.
55 A. Sen, S. Sharma, S. Dutta, M. M. Shirolkar, G. K. Dam, S. Let and S. K. Ghosh, *ACS Appl. Mater. Interfaces*, 2021, **13**, 34188–34196.
56 Z. Shang, F. Pu, X. Zhang, H. Jin, S. Chen, Y. Ding and A. Hu, *ACS Appl. Polym. Mater.*, 2023, **5**, 3827–3834.
57 D. Dai, J. Yang, Y.-C. Zou, J.-R. Wu, L.-L. Tan, Y. Wang, B. Li, T. Lu, B. Wang and Y.-W. Yang, *Angew. Chem., Int. Ed.*, 2021, **60**, 8967–8975.
58 X. Zhang, I. da Silva, R. Fazzi, A. M. Sheveleva, X. Han, B. F. Spencer, S. A. Sapchenko, F. Tuna, E. J. L. McInnes, M. Li, S. Yang and M. Schröder, *Inorg. Chem.*, 2019, **58**, 14145–14150.
59 K. Su, W. Wang, B. Li and D. Yuan, *ACS Sustainable Chem. Eng.*, 2018, **6**, 17402–17409.

